

Characterization of Noise and Resolution for Quantitative ^{177}Lu SPECT/CT with xSPECT Quant

Authors:

Dr. Johannes Tran-Gia*

Prof. Dr. Michael Lassmann

Affiliation:

Department of Nuclear Medicine

University of Würzburg

Oberdürrbacher Str. 6

97080 Würzburg, Germany

***Corresponding Author**

Phone: +49-931-201-35421

Email: Tran_J@ukw.de

Running Title:

Noise and Resolution Lu-177 xSPECT Quant

Word Count:

This manuscript contains 5,837 words.

ABSTRACT

Quantitative SPECT/CT imaging forms the basis for internal dosimetry in molecular radiotherapies. While the conversion from counts to activity is typically performed based on conversion factors individually measured by each site, a recently introduced commercially available reconstruction (xSPECT Quant) offers a standardized and traceable calibration of SPECT/CT systems. The aim of this work was to assess the characteristics of xSPECT Quant in combination with ^{177}Lu as one of the most important radionuclides used in molecular radiotherapies and to compare it to a widely used ordered subset expectation maximization reconstruction (Flash3D).

Methods

In a series of ^{177}Lu -filled phantom measurements, several important features were investigated for xSPECT Quant and Flash3D: Noise behavior and accuracy of the activity determination were evaluated in a large cylinder. Recovery coefficients were assessed in a hot-sphere phantom with and without background. Additionally, the resolutions were determined in a line source phantom as well as in a matched-filter resolution analysis of the hot-sphere-cold-background phantom.

Results

Both reconstruction algorithms improve the spatial resolution at the cost of noise build-up. Despite its slower convergence, Flash3D features a more efficient recovery. Although resolution recovery methods are applied within both reconstructions, partial volume errors – namely activity overestimation in the object center and spill-out of counts from the object edges – remain of relevance. In contrast to Flash3D where only the total number of updates (iterations×subsets) plays a role, the exact subdivision into iterations and subsets affected all characteristics of xSPECT Quant (optimum: 1 subset). The optimal trade-off between noise build-up and resolution improvement was found for 48 iterations and 1 subset, resulting in a quantitative accuracy of 1.2% in the Jaszczak cylinder (xSPECT Quant cross-calibrated to the dose calibrator).

Conclusion

If the reconstruction parameters are chosen with care, both examined reconstructions can provide absolute quantitative SPECT images with high image quality (sub-centimeter resolution at an acceptable noise build-up) as well as high quantitative accuracy (given a well-calibrated Flash3D conversion from counts to activity concentration). With its standardized (and traceable) activity determination, xSPECT Quant dispenses with site-specific calibration

protocols, enabling a reliable activity determination comparable across sites, which is especially useful for multi-centric molecular radiotherapy studies.

INTRODUCTION

Molecular radiotherapies are systemic therapies in which radionuclides or radiopharmaceuticals are administered to the patient. For many years, molecular radiotherapies have been performed with little or no consideration of patient-specific dosimetry or, if so, mainly at an organ level (1,2). Patient-specific dosimetry is, however, essential for a risk estimation prior to any treatment as well as an assessment of the safety and efficacy of a treatment (2). Besides the energy deposition patterns of the administered radionuclide in the patient, information about the time course of the activity distribution is needed for reliable dosimetry calculations. To obtain this information, sequential quantitative SPECT/CT, PET/CT or planar imaging is typically performed after the administration of the radiopharmaceutical (1). Based on this data, time-integrated activity coefficients in any volume-of-interest (VOI) are derived.

Although, in principle, SPECT/CT imaging offers the possibility of organ-based activity quantification, a large number of potential error sources have to be addressed before an accuracy adequate for standardized dosimetry calculations can be achieved (3,4). Most correction methods (e.g. attenuation correction, scatter correction, compensation for detector response, dead-time correction) are site-independent and should ideally be included in the reconstruction algorithm by the manufacturers. In contrast, the calibration of

each SPECT/CT system (i.e. the conversion from count rate to activity concentration) is camera-dependent. In this case, a system-specific conversion factor has to be individually determined by each site (5,6). Additionally, partial-volume errors represent a large source of error in SPECT/CT-based activity quantification (7): Image enhancement techniques seek to recover the resolution directly from the emission data (8-10). In contrast, image-domain correction techniques try to restore spilled-out counts based on anatomical information or pre-determined experimental findings, e.g. by multiplication with a spherical recovery coefficient (11,12) or more organ-specific correction factors obtained in anthropomorphic, 3D-printed phantoms (13-15). Although many efforts have been made to standardize quantitative SPECT/CT imaging (5,6,16,17), the lack of a widely accepted and routinely applied standardization still impedes a comparison of quantitative SPECT/CT acquisitions across different clinical centers and different manufacturers. This, in turn, obstructs the conduction of multi-centric or longitudinal studies for validating and optimizing the therapeutic use of new radiopharmaceuticals (18).

The use of a National Institute of Standards and Technology (NIST) traceable calibration source (^{75}Se) with a 3% uncertainty (99% confidence level) was recently introduced by Siemens Healthineers for medium energy radionuclides (^{123}I , ^{111}In , ^{177}Lu) to ensure standardization of quantitative

SPECT (19,20). In this new approach (“xSPECT Quant”), the reconstruction estimates the activity concentration (Bq/mL) in image space using the measured point spread function for the respective collimator class standard and energy window setting (site-independent) in combination with a system-specific sensitivity correction factor measured with a site-specific ^{75}Se point source. A cross-calibration to site-specific dose calibrators is supported by the software. As in PET imaging, the reconstructed images are provided in units of Bq/mL.

xSPECT Quant uses a pre-conditioned ordered subset conjugate gradient minimization of the Mighell’s modified chi-squared objective function (20,21), with different noise and convergence properties than the commonly applied expectation maximization optimization methods (22-24).

In this work, a series of ^{177}Lu -filled phantom measurements were performed to examine the influence of iterations and subsets on 1) the accuracy in activity determination, 2) the noise build-up, 3) the resolution improvement, and 4) the reduction of partial-volume effects (improvement of recovery coefficients). The results were compared with the results of an ordered subset expectation maximization (OSEM) based reconstruction (Flash3D). Conclusively, recommendations on the optimal combination of iterations and subsets are derived to facilitate the configuration of xSPECT Quant for Lu-177 SPECT/CT in molecular radiotherapies.

METHODS

Quantitative SPECT/CT imaging

All acquisitions were performed with a Symbia Intevo Bold SPECT/CT system (Siemens Healthineers) with 9.5mm crystal thickness, medium-energy low-penetration collimator, 180° configuration, auto-contouring, continuous mode, 60 views, 30s-per-view, 256×256-matrix, 3 energy windows (20% around the main photopeak of 208keV with two adjacent 10% windows). Subsequent to the SPECT acquisition, a low-dose CT was acquired for attenuation correction (130kVp, 512×512×131-matrix, 1.0×1.0×3.0mm³ resolution).

The following phantom experiments were performed:

- **Large Jaszczak cylinder** without inserts (diameter=21.6cm, height=18.6cm, volume=6.8L, activity concentration=73.5kBq/mL, total counts=8.0M) (25).
- Water-filled **body phantom** (NEMA-NU2-2012, PTW-Freiburg) equipped with 6 ¹⁷⁷Lu-filled **spheres** (diameters=10/13/17/22/28/37mm, activity concentration=1.31MBq/mL, total counts=4.2M). After the cold-background measurement, ¹⁷⁷Lu was added to the background and all acquisitions were repeated (21.1M total counts). Subsequent to these

acquisitions, 1mL aliquots of the sphere and the background solutions were measured in the HPGe detector, yielding a sphere-to-background activity ratio of 10.1:1.0.

- Water-filled **head phantom** (IEC-61675-2, PTW-Freiburg) equipped with 2 ^{177}Lu -filled line sources (diameter=1mm, length=17.5cm, total activity \approx 300MBq, average total counts=7.4M) placed in the center and 9cm off-center. The phantom was rotated between four subsequent acquisitions to measure the transaxial resolution at the center and at the 12 (anterior), 3 (right), 6 (posterior), and 9 o'clock position (left).

Reconstructions were performed with the following 2 algorithms, applied without and with 16mm 3D Gaussian post-filtering (one of the most frequent post-filters applied within the manufacturer's reconstruction presets) with varying combinations of iterations and subsets ('48i1s': 48 iterations, 1 subset):

- **Flash3D**: OSEM with depth-dependent 3D resolution recovery (Gaussian PSF model), attenuation correction, and scatter correction. Reconstructions were performed with a 128 \times 128-matrix as recommended by the manufacturer (voxel size=4.8mm). For quantitative imaging, a count-to-activity conversion factor cf [cps/MBq] was manually determined (cps: counts-per-second) (4,26).

- **xSPECT Quant:** Ordered subset conjugate gradient minimization with depth-dependent 3D resolution recovery using a measured PSF, attenuation correction, additive data driven scatter correction in forward projection, and decay correction. As recommended by the manufacturer, a 256×256 -matrix was used for the reconstruction (voxel size=2.0mm). For simplicity, *xSPECT Quant* will be called *xSPECT*.

Attenuation and scatter correction were applied according to the manufacturer-suggested settings. Activities were determined using a VDC-405 dose calibrator with a VIK-202 ionization chamber (Comcer SpA), cross-calibrated to a high-purity germanium detector (HPGe; Canberra Industries Inc.) whose energy-dependent efficiency was calibrated with several NIST and National Physical Laboratory traceable standards over the energy range considered. All xSPECT-based activities were cross-calibrated to this dose calibrator by applying a pre-measured cross-calibration factor of $A_{\text{DoseCalibrator}}/A_{\text{NIST}}=1.025$ ($A_{\text{DoseCalibrator}}$: dose calibrator activity, A_{NIST} : xSPECT-based activity). Activity concentrations were determined based on weight. To ensure a homogeneous distribution of the radionuclides, ^{177}Lu chloride was dissolved in 0.1M HCl with 100ppm stable Lu for all measurements. Post-processing was performed in MATLAB R2016b (The MathWorks) and MI Applications VA60C (Siemens Healthineers).

Conversion Factor & Accuracy

The Jaszczak data were used to determine the Flash3D conversion factor cf and assess the accuracy of the xSPECT-based activity determination. First, cf was determined based on the total number of counts in a cylinder VOI_{outside} containing the entire phantom (diameter=23.6cm, height=20.6cm, volume=9.0L):

$$cf = \frac{\text{counts}}{\text{total activity} \cdot \text{time}} \left[\frac{\text{cps}}{\text{MBq}} \right] \quad [1]$$

The same VOI was used to obtain the activity based on xSPECT (Bq/mL in $VOI_{\text{outside}} \times \text{volume}$). Additionally, a cylinder VOI_{inside} (diameter=14.5cm, height=12.5cm, volume=2.1L) was drawn inside the phantom to assess the accuracy of the xSPECT-based activity concentration (Bq/mL in VOI_{inside}).

Update-Dependency of Noise

The Jaszczak data were used to assess the noise build-up of both reconstruction algorithms as a function of updates (iterations \times subsets). For this purpose, the noise coefficient of variation (CV) was calculated as ratio between standard deviation and mean of VOI_{inside} . To account for variations inside the

phantom, the VOI was shifted across 5 voxels in all dimensions, and the average of the resulting 125 values of noise CV was taken.

Sphere-Based Recovery Coefficients

To assess the update-dependent influence of partial-volume errors on the activity determination, recovery coefficients were calculated based on the sphere phantom data: First, a set of spherical VOIs was manually drawn (diameters based on the phantom specifications, CT-based positioning) and the SPECT-based activity A_{SPECT} inside these VOIs was determined. Subsequently, recovery coefficients were calculated based on the nominal activity $A_{DoseCalibrator}$ in each sphere (11):

$$RC = \frac{A_{SPECT}}{A_{DoseCalibrator}} \quad [\quad] \quad]$$

Line Source Resolution Analysis

The spatial resolution was investigated based on the line source data. After interpolating the reconstructed SPECT volumes by a factor of 10 (grid sizes=0.48/0.20mm [Flash3D/xSPECT]), the sagittal and coronal full-width at half-maximum (FWHM) was first extracted for all available slices. By averaging 1) over the central ~12cm of slices containing the line phantom, 2)

over sagittal and coronal resolutions, and 3) over all four rotated acquisitions, center and off-center resolution values were obtained.

Matched-Filter Resolution Analysis

A matched-filter resolution analysis of the sphere phantom data was performed as follows (27,28): First, a digital version of the phantom was derived by CT-based thresholding. Next, SPECT-based resolution loss was simulated by convolution with 3D Gaussian kernels of different FWHMs. After resampling to SPECT matrix size, the minimum root-mean-squared errors (RMSEs) between the reconstructed and the simulated volumes were calculated to find a resolution estimate. While the mask's background was set to zero for the hot-sphere-cold-background experiment, the background activity was adjusted to achieve the predetermined sphere-to-background ratio of 10.1:1.0 in the hot-sphere-hot-background case.

RESULTS

Update-Dependency of the Quantitative Accuracy

The update-dependency and the effect of post-filtering are illustrated in Figure 1 by cross-sections through the Jaszczak phantom. Additionally, example Flash3D conversion factors as well as xSPECT-based activities A_{SPECT} ($\text{VOI}_{\text{outside}}$) and activity concentrations C_{SPECT} ($\text{VOI}_{\text{inside}}$) are given in Tables 1 and 2 (the uncertainty of A_{SPECT} was estimated based on a Poisson distribution $1/\sqrt{\text{Total Counts}}$).

On the one hand, the contours of the initially blurred edges (green curves) are sharpened by more updates, reducing spill-out for $\text{VOI}_{\text{outside}}$ (solid black line). This is underlined by the conversion factors cf (Table 1), where the spill-out initially leads to a $\sim 7\%$ lower cf (6i1s), which is improved by more updates ($>48i1s$).

On the other hand, a growing number of updates results in an increasing noise build-up and pronounced Gibbs ringing (blue and red curves). cf (Flash3D) and A_{SPECT} (xSPECT), however, are nearly unaffected by the high noise (Tables 1 and 2).

While the noise inside the phantom is considerably reduced by the post-filter (Figures 1C and 1D), it reintroduces blurring to the edges, leading to spill-

out of counts from VOI_{outside} (orange arrows) for Flash3D. In contrast, this effect does not occur for xSPECT (magenta arrows). While no systematic changes are introduced by the post-filter for cf (Flash3D + VOI_{outside}) and C_{SPECT} (xSPECT + VOI_{inside}), the 1%-2% difference of A_{SPECT} (xSPECT + VOI_{outside}) is systematically increased to 3%-4%.

Update-Dependency of the Noise Build-Up

The update-dependent noise build-up inside the Jaszczak phantom is shown in Figure 2A. Two observations can be made: 1) While the noise build-up is independent of the number of subsets for Flash3D (red curves), a clear subset-dependency (e.g., a factor of 1.75 between 72i1s and 12i6s indicated by the orange boxes) is visible for xSPECT (blue curves). 2) xSPECT features a faster noise build-up than Flash3D. This is underlined by an average factor of 2.2 between the noise CV of Flash3D and xSPECT for 1 subset, which increases to 3.1 for 6 subsets (blue divided by red curves).

Subset-Dependency of xSPECT

To further illustrate the subset-dependency of xSPECT, Figure 2B plots the number of subsets against the noise CV inside the Jaszczak phantom for a fixed number of 48 updates. While the noise is subset-independent in Flash3D

(red solid line, 9% average), the noise build-up increases with the number of subsets in xSPECT (blue solid line, 20%→38% increase). While the noise is considerably reduced by the post-filtering (dashed lines, average: 2.0/3.2-fold for Flash3D/xSPECT, the subset-dependency of xSPECT is preserved (5% average for Flash3D versus 7%→14% increase for xSPECT).

This subset-dependency is further visualized by Figure 3 (constant update number): While the cross-sections remain unchanged for Flash3D (Figures 3A and 3C), a subset-dependent noise increase can be seen for xSPECT (Figure 3B). Although the noise is considerably reduced by the post-filter, the subset-dependency of xSPECT is preserved (Figure 3D). Again, the spill-out introduced by the post-filtering for Flash3D does not occur for xSPECT.

Sphere-Based Recovery Coefficients

Although the results will not be explicitly given here, a subset-dependency was again only found for xSPECT. Therefore, the number of subsets was kept at 1 throughout the following recovery coefficient analysis.

The volume-dependent recovery coefficients RC are shown in Figure 4A. For clarity, only the reconstructions with 48i1s are plotted. Without filter and background (solid lines), the recovery of Flash3D exceeds xSPECT by an average factor of ~ 1.2 . While both reconstructions start with an RC of ~ 0.2 for

the smallest sphere (0.6mL), Flash3D features a considerably faster recovery (e.g., an RC of 0.7 is reached for the 2.8mL/11.4mL sphere for Flash3D/xSPECT). Both recoveries are considerably deteriorated in the presence of background.

To visualize the update-dependency of the recovery coefficients, RC s of the largest sphere (diameter=37mm, volume=26.5mL) for different iterations and 1 subset are shown in Figure 4B. Again, it can be seen that Flash3D converges towards a higher RC (without/with background: 0.89/0.83) than xSPECT (0.82/0.79). While an average improvement of 89% is reached between iterations 6 and 48, only a negligible further improvement of 8% is reached between 48 and 96 iterations.

To visualize the impact of update number and background on the reconstructions, Figure 5 shows cross-sections through the largest sphere for different update numbers. The nominal dimensions and activity concentrations are indicated by the orange dashed boxes. Without background, the activity concentration outside the sphere goes down to zero for both reconstructions. While the reconstructed background concentration reaches the nominal value on both sides of the sphere for Flash3D, it becomes strongly asymmetric for xSPECT (curves versus solid orange boxes).

Additionally, the background has a large influence on the updates needed to recover the resolution: Without background, a maximum is reached after 24 (Flash3D, blue curve) and 72 (xSPECT, magenta curve) updates; the concentration starts to deteriorate with an increasing number of updates. With background, however, the resolution of both reconstructions is still under improvement after 96 updates.

To illustrate the distribution of activity inside the sphere VOIs, the activity concentrations in the “hottest” milliliter C_{\max} (~ 125 voxels) of the largest sphere are given in Table 3. While the concentration without background is close to the nominal value of 1.31MBq/mL at the start of the reconstruction (e.g., 61s), it is increasingly overestimated with more iterations. In contrast, the initial values considerably underestimate the nominal concentration after the addition of background activity ($-24\%/ -61\%$ for xSPECT/Flash3D). Similar to the non-background case, an overestimation occurs after several iterations.

Resolution Analysis

Figure 6 shows the matched-filter resolutions plotted against the number of updates. Generally, post-filtering leads to a considerable decrease in resolution (average: 1.87/1.65-fold for Flash3D/xSPECT). Differences between

hot/cold background resolutions occur only in the unfiltered Flash3D case (solid lines) and in the filtered xSPECT case (dashed lines).

All resolutions are additionally listed in Table 4. For clarity, post-filtering and background are not listed. For all reconstructions, the spatial resolution is considerably improved by an increasing number of updates (average improvement 17.8mm→6.6mm in the analyzed range). This is further illustrated by the average resolution improvement (ratio of mean resolutions after 6i1s and XiXs) given in the last column. While the resolution is improved by a factor of 2.0 for 48 updates, it is only further improved to 2.7 for 576 updates. As expected, the off-center line source resolution exceeds the center resolution for both reconstruction methods (average factor of 1.2/1.6 for Flash3D/xSPECT).

As Flash3D and xSPECT feature a different convergence behavior, Figure 7 depicts the noise-dependency of the resolution. While only small differences occur between matched-filter and center line source (cyan versus red, average: $-0.4\%/ -2.4\%$ for Flash3D/xSPECT), differences are more pronounced between off-center line source and matched-filter (green versus cyan, average: $-17.1\%/ 37.4\%$ for Flash3D/xSPECT). While no subset-dependency is visible for Flash3D, a clear noise increase can be observed

between 1 and 6 subsets for xSPECT (horizontal shift of solid lines against dashed lines).

DISCUSSION

Our results demonstrate a high quantitative accuracy of xSPECT Quant for ^{177}Lu without the need for an in-house calibration protocol. However, a large number of differences to the widely used OSEM-based Flash3D reconstruction became evident which will be discussed below to facilitate clinical implementation.

Update-Dependency of the Quantitative Accuracy

After 61s, the resolution of Flash3D is insufficiently recovered, leading to partial-volume effects at the object edges and, therefore, an underestimation of cf (Table 1). This is successfully corrected in the course of the reconstruction (i.e. with more updates). Although Gibbs ringing artifacts and noise become more pronounced especially at the object edges, the inclusion of all counts spilling out of the Jaszczak phantom ($\text{VOI}_{\text{outside}}$) and the related averaging ensures that cf and A_{SPECT} hold even for large update numbers such as 9616s. Accordingly, the lowest difference of 1.2% to the dose calibrator was reached for $\text{VOI}_{\text{outside}}$, outperforming the accuracies of previously published quantification approaches (Table 5).

The signal variations across the cross-section in Figure 1 illustrate that the increasing noise build-up eventually plays a larger role for decreasing phantom

or VOI sizes. For large phantoms such as the Jaszczak phantom, the concentration-based activity determination with VOI_{inside} (or any other VOI smaller than the phantom volume) becomes increasingly position-dependent. Consequently, the VOI_{inside} -based accuracy was worse than the VOI_{outside} -based accuracy for all reconstructions (Table 2).

The fact that spill-out is introduced by the post-filter for Flash3D but not for xSPECT (Figure 1D) can be explained by a CT-based intensity masking that is applied by the manufacturer as a constraint for the spatial distribution of counts within xSPECT. The fact that systematic changes in quantitative accuracy are introduced by the post-filter only for xSPECT in combination with VOI_{outside} (Table 2) suggests that they originate in the phantom's edge area and that they might, therefore, also be related to the CT-based masking. As details about the reconstruction engine are not publicly available, however, this only represents one potential explanation. Further in-depth studies will be needed for a well-founded assessment of this effect.

Update-Dependency of the Noise Build-Up

As expected, the noise level of both reconstruction methods increases with the number of updates (Figure 2A). The 2.2/3.1-fold higher noise build-up of xSPECT (1s/6s) originates from the faster convergence of the conjugate

gradient based optimization (xSPECT) compared to expectation maximization (Flash3D) (22,23). As the subdivision of updates into iterations and subsets has no effect on the noise in Flash3D (Figures 3A and 3C), the number of subsets can be increased to accelerate the reconstruction. In contrast, xSPECT should preferably be carried out with only 1 subset to minimize noise (Figures 2B, 3B and 3D). Although only one noise level (i.e. the activity concentration inside the Jaszczak phantom) was investigated in this work, the informative value of the noise-versus-resolution curve (Figure 7) will remain the same for different noise levels. For lower/higher noise levels, the curve would be horizontally compressed/uncompressed towards the lower/higher noise regime, respectively.

Sphere-Based Recovery Coefficients

In general, the recovery coefficients of both reconstruction methods increase with volume and number of updates (Figure 4). Without background, Flash3D – despite its slower convergence – features a more effective recovery than xSPECT for all volumes and update numbers. As the largest portion of the maximum recovery is already reached after 48 of the 96 depicted updates (Figure 4B), the combination 48i1s appears to be a good compromise between resolution recovery and noise build-up.

The addition of background leads to smaller recovery coefficients, which can be explained by a noise-dependent convergence behavior: The background noise reduces the algorithm’s “confidence” in the reconstruction, in turn leading to an increased number of updates needed to achieve a resolution similar to the background-free case, of course at an increased noise level. While the background activity concentration is reliably restored for Flash3D, it asymmetrically varies around the sphere and even reaches zero at several locations for xSPECT (Figure 5), potentially leading to errors in the matched-filter resolution analysis.

The hottest milliliter analysis of both reconstructions (Table 3) shows that, instead of recovering a clear edge separating the constant activity concentration inside the sphere from the background (orange dashed boxes in Figure 5), the activity is overestimated in the sphere center to compensate for the counts spilled out of the sphere edges. As the recovery coefficients approach the nominal value (which is equal to 1 for ideal imaging conditions), the activity concentrations are overestimated by up to a maximum factor of ~ 2 . Although both reconstruction engines feature resolution recovery methods, partial volume errors – especially spill-out for hot objects – thus remain relevant in any VOI-based quantitative analysis. If a voxel-based analysis is to

be performed (e.g. in voxel-based dose assessments), even dedicated partial-volume correction methods might become necessary.

Resolution Analysis

For both reconstruction algorithms, the resolution is considerably improved by an increasing number of updates (Figure 6). The resolution difference for unfiltered Flash3D with and without background can be explained by the different convergence behavior in the presence of background (Figure 5). This difference is considerably softened by the post-filter, leaving only negligible differences. In contrast, a difference occurs after post-filtering for xSPECT. As explained in the previous section, this might be caused by the asymmetric background activity especially in the edge regions, in turn leading to errors in the matched-filter resolution analysis.

Line-based resolution measurements enable the location-dependent assessment of spatial resolution, which is especially useful for SPECT imaging where the resolution is dependent on the object-detector distance. These methods were, however, previously reported to potentially introduce systematic errors for iterative reconstructions including distance-dependent resolution corrections (29). Without the need of an in-depth model of the image formation process, matched-filter approaches represent a powerful and reconstruction-

independent alternative for SPECT resolution assessments. As they return an average resolution defined by all transitions between different activity concentrations in the measured field-of-view, they do not provide sufficient information for a systematic assessment of the spatial resolution. Therefore, a combination of both methods was applied:

- *Line-based method*: Assesses the location-dependency of the spatial resolution (e.g. differences between centric and off-centric positioning).
- *Matched-filter method*: Validates the line-based resolution values.

The good agreement between both methods suggests that the line source measurement represents a suitable means for assessing orientation- and position-dependent changes in spatial resolution. The fact that the matched-filter (NEMA sphere phantom) resolutions mainly lie between the 9cm off-center (better) and center (worse) line source resolutions are explained by the average off-center distance of the NEMA spheres, which was approximately between both line source positions (less than 9cm off-center). As the matched-filter resolution is independent of the location, a more detailed numerical comparison makes no sense.

Finally, the orange circles in Figure 7 indicate update numbers with an optimal trade-off between resolution recovery and noise-build-up for the matched-filter resolution (cyan curves, ~48/24 updates for Flash3D/xSPECT).

For higher update numbers, the noise increase outweighs the resolution improvement. This is in good agreement with the optimal iteration-subset combination of 48i1s determined in the recovery coefficient discussion in the previous section.

CONCLUSION

In this work, the recently introduced xSPECT Quant reconstruction for absolute quantitative SPECT imaging (output: Bq/mL) was compared against the widely used Flash3D reconstruction (output: counts). If the reconstruction parameters are chosen with care, both reconstructions can provide absolute quantitative SPECT images with comparable image quality (noise build-up and resolution recovery) as well as comparable quantitative accuracy (given a well-calibrated Flash3D conversion from counts to activity concentration). The most important advantages of the Flash3D reconstruction are a more effective recovery of the activity (despite the slower convergence) and the fact that subsets can be increased to speed up reconstruction time (no subset-dependency). For the conjugate gradient based xSPECT Quant reconstruction, in contrast, all investigated reconstruction parameters were dependent on the number of subsets (1 subset: least noise). Additionally, xSPECT Quant features a faster convergence (at the cost of a higher noise build-up) and applies a CT-derived reconstruction mask for background noise reduction. Most importantly, however, xSPECT Quant provides a reliable, NIST traceable quantification with minimal calibration effort, which is independent of the site-specific technical expertise. If adequate partial-volume corrections are applied, xSPECT Quant holds the potential for standardized quantitative SPECT/CT imaging,

enabling quantitative imaging and, thus, the calculation of absorbed doses that are comparable across multiple sites. An optional dose calibrator cross-calibration enables each site to directly compare the activities determined by SPECT/CT with injected activities or other liquid patient samples (e.g. urine or blood samples). Therefore, xSPECT Quant represents a major step towards a standardized and traceable absolute quantification in ^{177}Lu SPECT/CT imaging, as it is already standard in PET/CT imaging.

ACKNOWLEDGEMENT

The authors would like to thank A. H. Vija and J. Zeintl for very helpful comments.

DISCLOSURE

No potential conflicts of interest relevant to this article exist.

FUNDING

This work was partly supported by the European Metrology Programme for Innovation and Research (EMPIR) project 16HLT06 MRTDosimetry (<http://mrtdosimetry-empir.eu/>). The EMPIR is jointly funded by the EMPIR participating countries within EURAMET and the European Union.

REFERENCES

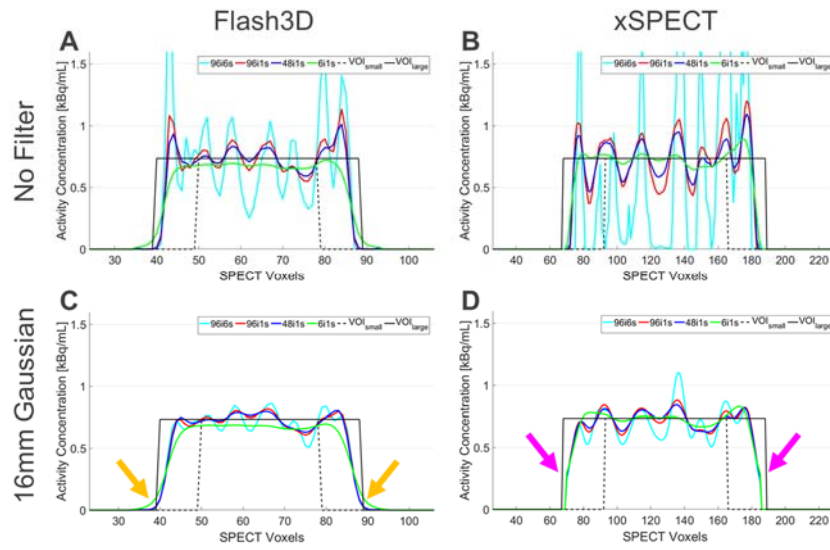
1. Stabin MG. *Fundamentals of nuclear medicine dosimetry*. New York, NY: Springer Science & Business Media; 2008.
2. Glatting G, Lassmann M. Nuclear medicine dosimetry: quantitative imaging and dose calculations. *Z Med Phys*. 2011;21:246-247.
3. Dewaraja YK, Frey EC, Sgouros G, et al. MIRD Pamphlet No. 23: Quantitative SPECT for patient-specific 3-dimensional dosimetry in internal radionuclide therapy. *J Nucl Med*. 2012;53:1310-1325.
4. Ljungberg M, Celler A, Konijnenberg MW, Eckerman KF, Dewaraja YK, Sjögreen-Gleisner K. MIRD Pamphlet No. 26: Joint EANM/MIRD guidelines for quantitative ^{177}Lu SPECT applied for dosimetry of radiopharmaceutical therapy. *J Nucl Med*. 2016;57:151-162.
5. D'Arienzo M, Cazzato M, Cozzella ML, et al. Gamma camera calibration and validation for quantitative SPECT imaging with ^{177}Lu . *Appl Radiat Isot*. 2016;112:156-164.
6. Uribe CF, Esquinas PL, Tanguay J, et al. Accuracy of ^{177}Lu activity quantification in SPECT imaging: a phantom study. *EJNMMI Phys*. 2017;4:2.
7. Erlandsson K, Buvat I, Pretorius PH, Thomas BA, Hutton BF. A review of partial volume correction techniques for emission tomography and their applications in neurology, cardiology and oncology. *Phys Med Biol*. 2012;57:R119-159.
8. Tsui BM, Frey EC, Zhao X, Lalush DS, Johnston RE, McCartney WH. The importance and implementation of accurate 3D compensation methods for quantitative SPECT. *Phys Med Biol*. 1994;39:509-530.
9. Hutton BF, Lau YH. Application of distance-dependent resolution compensation and post-reconstruction filtering for myocardial SPECT. *Phys Med Biol*. 1998;43:1679-1693.
10. Teo BK, Seo Y, Bacharach SL, et al. Partial-volume correction in PET: validation of an iterative postreconstruction method with phantom and patient data. *J Nucl Med*. 2007;48:802-810.

11. Hoffman EJ, Huang SC, Phelps ME. Quantitation in positron emission computed tomography: 1. Effect of object size. *J Comput Assist Tomogr.* 1979;3:299-308.
12. Willowson K, Bailey DL, Baldock C. Quantitative SPECT reconstruction using CT-derived corrections. *Phys Med Biol.* 2008;53:3099-3112.
13. Tran-Gia J, Schlögl S, Lassmann M. Design and fabrication of kidney phantoms for internal radiation dosimetry using 3D printing technology. *J Nucl Med.* 2016;57:1998-2005.
14. Tran-Gia J, Lassmann M. Optimizing image quantification for ^{177}Lu SPECT/CT based on a 3D printed 2-compartment kidney phantom. *J Nucl Med.* 2018;59:616-624.
15. Robinson AP, Tipping J, Cullen DM, et al. Organ-specific SPECT activity calibration using 3D printed phantoms for molecular radiotherapy dosimetry. *EJNMMI Phys.* 2016;3:12.
16. Sanders JC, Kuwert T, Hornegger J, Ritt P. Quantitative SPECT/CT imaging of ^{177}Lu with in vivo validation in patients undergoing peptide receptor radionuclide therapy. *Mol Imaging Biol.* 2015;17:585-593.
17. Zimmerman BE, Grošev D, Buvat I, et al. Multi-centre evaluation of accuracy and reproducibility of planar and SPECT image quantification: An IAEA phantom study. *Z Med Phys.* 2017;27:98-112.
18. Flux G, Bardies M, Monsieurs M, Savolainen S, Strands SE, Lassmann M. The impact of PET and SPECT on dosimetry for targeted radionuclide therapy. *Z Med Phys.* 2006;16:47-59.
19. Vija H. Introduction to xSPECT technology: Evolving multi-modal SPECT to become context-based and quantitative. Siemens Medical Solutions USA. 2014.
20. Vija AH. Characteristics of the xSPECT reconstruction method. Siemens Medical Solutions USA, Inc., Molecular Imaging, White Paper. 2017.

21. Mighell KJ. Parameter estimation in astronomy with Poisson-distributed data. II. The modified chi-square-gamma statistic. *arXiv preprint astro-ph/0007328*. 2000.
22. Tsui B, Zhao X, Frey E, Gullberg G. Properties of iterative algorithms in SPECT image reconstruction. Paper presented at: Nuclear Science Symposium, 1990. Conference record: Including Sessions on Nuclear Power Systems and Medical Imaging Conference, 1990 IEEE, 1990.
23. Tsui B, Zhao X, Frey E. Comparison between ML-EM and WLS-CG algorithms for SPECT image reconstruction. *IEEE Trans Nucl Sci*. 1991;38:1766-1772.
24. Wilson DW, Tsui BM, Barrett HH. Noise properties of the EM algorithm: II. Monte Carlo simulations. *Phys Med Biol*. 1994;39:847-871.
25. Jaszczak RJ. Nuclear imaging phantom. U.S. Patent No. 4,499,375; 1985.
26. Zeintl J, Vija AH, Yahil A, Hornegger J, Kuwert T. Quantitative accuracy of clinical ^{99m}Tc SPECT/CT using ordered-subset expectation maximization with 3-dimensional resolution recovery, attenuation, and scatter correction. *J Nucl Med*. 2010;51:921-928.
27. Cunningham IA, Fenster A. A method for modulation transfer function determination from edge profiles with correction for finite-element differentiation. *Med Phys*. 1987;14:533-537.
28. Ma J, Vija AH. Evaluation of quantitation accuracy for xSPECT. Paper presented at: Nuclear Science Symposium and Medical Imaging Conference (NSS/MIC), 2015 IEEE, 2015.
29. Badger D, Barnden L. Spatial resolution is dependent on image content for SPECT with iterative reconstruction incorporating distance dependent resolution (DDR) correction. *Australas Phys Eng Sci Med*. 2014;37:551-557.
30. Beauregard JM, Hofman MS, Pereira JM, Eu P, Hicks RJ. Quantitative ^{177}Lu SPECT (QSPECT) imaging using a commercially available SPECT/CT system. *Cancer Imaging*. 2011;11:56-66.

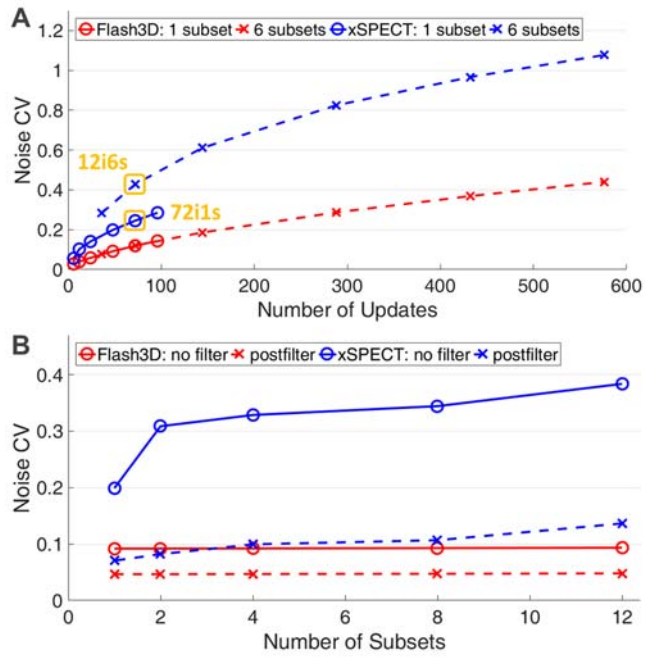
- 31.** de Nijs R, Lagerburg V, Klausen TL, Holm S. Improving quantitative dosimetry in ^{177}Lu -DOTATATE SPECT by energy window-based scatter corrections. *Nucl Med Commun.* 2014;35:522-533.
- 32.** Mezzenga E, D'Errico V, D'Arienzo M, et al. Quantitative accuracy of ^{177}Lu SPECT imaging for molecular radiotherapy. *PLoS One.* 2017;12:e0182888.
- 33.** Shcherbinin S, Piwowska-Bilska H, Celler A, Birkenfeld B. Quantitative SPECT/CT reconstruction for ^{177}Lu and $^{177}\text{Lu}/^{90}\text{Y}$ targeted radionuclide therapies. *Phys Med Biol.* 2012;57:5733-5747.

FIGURE 1



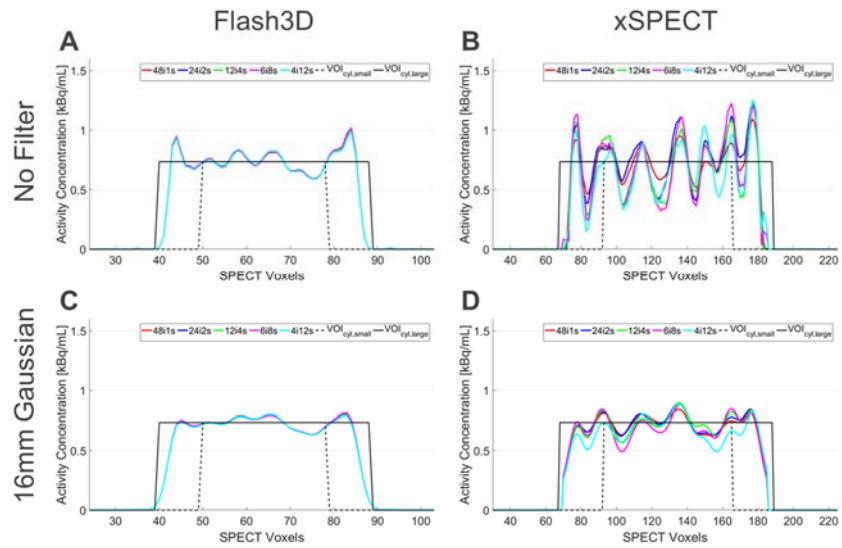
Cross-sections through the reconstructed Jaszczak phantom for different update numbers and post-filters. Solid/dashed black lines: $VOI_{\text{outside}}/VOI_{\text{inside}}$.

FIGURE 2



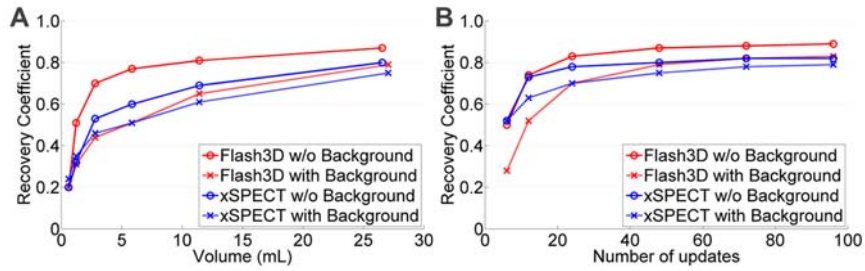
Update- (A) and subset-dependency (B) of the noise coefficient of variation for Flash3D (red) and xSPECT (blue).

FIGURE 3



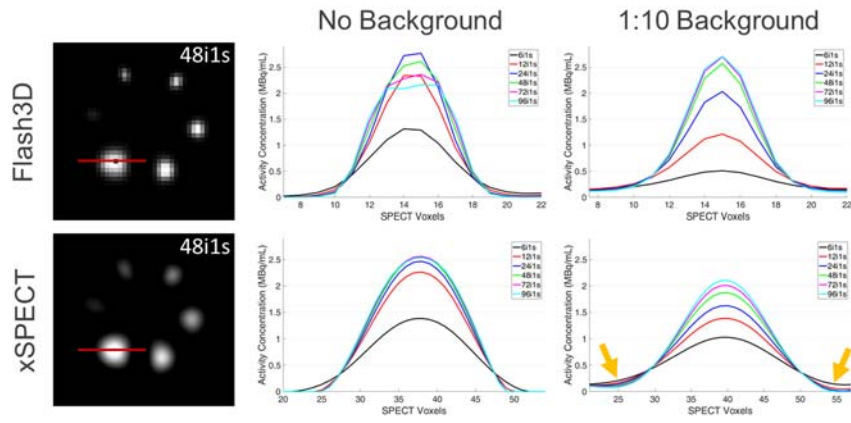
Cross-sections through the reconstructed Jaszczak phantom for different iteration-subset combinations and post-filters. Solid/dashed black lines: VOI_{outside}/VOI_{inside}.

FIGURE 4



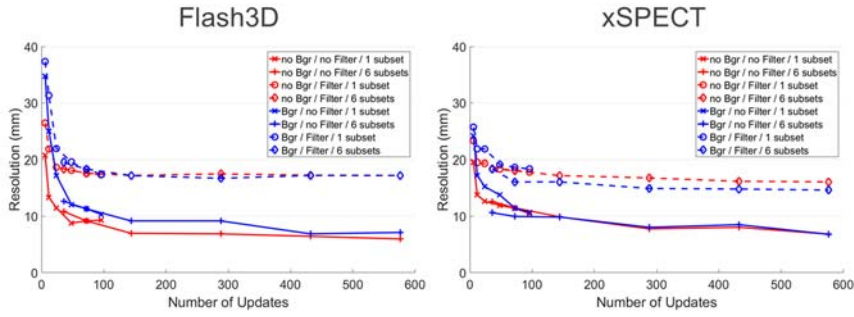
A: Volume-dependency of the recovery coefficient for 481s. B: Update-dependency of the recovery coefficient on the example of the largest sphere (number of updates: 1 subset \times different number of iterations). Red/blue color: Flash3D/xSPECT. Solid/dashed lines: cold/hot background.

FIGURE 5



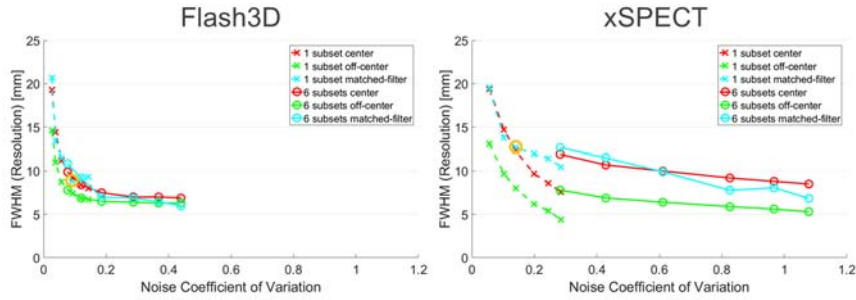
Example images of the NEMA sphere reconstructions (left) and cross-sections through the largest sphere (center/right: cold/hot background) for different iteration numbers.

FIGURE 6



Update-dependency of matched-filter resolution for 1/6 subsets. Red/blue: cold/hot background. Solid/dashed lines: no/16mm-Gaussian post-filter.

FIGURE 7



Noise-dependency of the resolution obtained from matched-filter (cyan) and line-based methods (red: center, green: 9cm off-center).

TABLE 1

Flash3D conversion factor *cf.* $A_{\text{DoseCalibrator}}=488.4\text{MBq}$, acquisition duration=1,800s.

	No Filter				16mm Gaussian Post-filter			
	6i1s	48i1s	96i1s	96i6s	6i1s	48i1s	96i1s	96i6s
Counts in VOI _{outside}	165.8M	178.8M	179.0M	179.7M	163.7M	177.5M	177.6M	177.9M
<i>cf</i> (cps/MBq)	18.86	20.33	20.36	20.44	18.62	20.19	20.21	20.23

TABLE 2

xSPECT activity $A_{\text{SPECT}}(\text{VOI}_{\text{outside}})$ and concentration $C_{\text{SPECT}}(\text{VOI}_{\text{inside}})$.
 $A_{\text{DoseCalibrator}}=490.6\text{MBq}$, $C_{\text{DoseCalibrator}}=73.5\text{kBq/mL}$ (both decay-corrected to
time of phantom preparation).

	No Filter				16mm Gaussian Post-filter			
	6i1s	48i1s	96i1s	96i6s	6i1s	48i1s	96i1s	96i6s
$\text{VOI}_{\text{outside}}$								
$A_{\text{SPECT}}(\text{MBq})$	500.3(2)	496.5(2)	496.9(2)	498.2(2)	509.5(2)	506.2(2)	506.9(2)	508.3(2)
Difference to $A_{\text{DoseCalibrator}}(\%)$	2.0	1.2	1.3	1.6	3.8	3.2	3.3	3.6
$\text{VOI}_{\text{inside}}$								
$C_{\text{SPECT}}(\text{kBq/mL})$	75.1	76.0	76.1	75.1	75.3	75.6	75.8	75.6
Difference to $A_{\text{DoseCalibrator}}(\%)$	2.2	3.3	3.5	2.2	2.5	2.9	3.2	2.9

TABLE 3

Maximum-milliliter activity concentration C_{\max} of the largest sphere for different iterations and 1 subset (MBq/mL).

Algorithm	Background	6i1s	12i1s	24i1s	48i1s	72i1s	96i1s
xSPECT	Cold	1.36	2.21	2.41	2.49	2.50	2.47
	Hot (10:1)	1.00	1.35	1.59	1.83	1.96	2.05
Flash3D	Cold	1.32	2.34	2.77	2.63	2.48	2.34
	Hot (10:1)	0.51	1.21	2.03	2.58	2.70	2.71

TABLE 4

Iteration-dependent resolutions (mm) and average resolution improvement Δr (ratio to 6i1s).

	Flash3D			xSPECT			Δr
	Line Source		Matched- Filter	Line Source		Matched- Filter	
	Center	Off-Center		Center	Off-Center		
6i1s	19.3	14.6	20.7	19.4	13.1	19.5	1.0
12i1s	14.4	11.0	13.4	14.7	9.7	13.8	1.4
24i1s	11.2	8.7	11.5	12.3	8.0	12.7	1.7
48i1s	9.2	7.4	8.8	9.7	6.2	12.0	2.0
72i1s	8.4	6.9	9.2	8.6	5.4	11.4	2.1
96i1s	8.0	6.7	9.3	7.6	4.4	10.5	2.3
6i6s	9.9	7.8	10.9	11.9	7.8	12.6	1.8
12i6s	8.4	6.9	9.2	10.7	6.9	11.5	2.0
24i6s	7.5	6.5	7.0	10.0	6.4	9.9	2.3
48i6s	7.0	6.4	6.9	9.2	5.9	7.8	2.5
72i6s	7.0	6.3	6.5	8.8	5.6	8.1	2.5
96i6s	6.9	6.3	6.0	8.5	5.3	6.8	2.7

TABLE 5Literature on ^{177}Lu SPECT/CT based activity determination.

Authors	Phantom Geometry	Volume	System	Reconstruction	Reported Accuracy
This Study	Cylinder	6.8L	Siemens	Manufacturer	1.2%
Beauregard et al. (30)	Cylinder	175mL to 2.5L	Siemens	In-House	~5.6%
D'Arienzo et al. (5)	Cylinder	4.2L	Philips	Manufacturer	3.7% and -11.6% (2 Systems)
de Nijs et al. (31)	Sphere	26.5mL	Philips	Manufacturer	~6.6%
Mezzenga et al. (32)	Cylinder	6.4L	GE	Manufacturer	~16.4%
Sanders et al. (16)	Spheres	0.5mL to 16.0mL	Siemens	Manufacturer	~20% (very small volumes)
Shcherbinin et al. (33)	Cylinder	70mL	GE	In-House	2%
Uribe et al. (6)	Spheres and Bottles	113mL to 199mL	Siemens	In-House	<5% (Objects>100mL)